Materials Horizons

Acoustic Metamaterials for Remote Manipulation of Large Objects in Water

Journal:	*Materials Horizons*
Manuscript ID	MH-COM-01-2025-000048.R1
Article Type:	Communication
Date Submitted by the Author:	02-Apr-2025
Complete List of Authors:	Zhang, Dajun; University of Wisconsin-Madison, Electrical and Computer Engineering Ma, Chu; University of Wisconsin-Madison, Department of Electrical and Computer Engineering

New concept statement

The acoustic wave scattering from a thin layer of metamaterial coated on an object's surface can generate radiation forces with tailored spatial distributions, enabling remote object manipulation. While this concept was demonstrated in air, it has not been extended to liquid environments due to the lack of underwater metamaterials with high acoustic impedance contrast with water and high fabrication resolution at the same time. Our work addresses this challenge by developing a new metamaterial fabrication technique using soft lithography of a metal-resin composite. The fabricated metamaterial enables the excitation of various actuation forces in water. Novel designs of the metamaterials are further developed to enable the simultaneous excitation of multiple forces from one single metamaterial layer, offering unprecedented maneuvering complexity and flexibility. Different from existing in-water acoustic manipulation systems that only works for objects comparable or smaller than the wavelength, our metamaterial-assisted system achieves 3D multi-path, multi-object, and non-invasive manipulation of objects larger than 20 times the wavelength. Our work will provide a new way to reduce the weight, complexity, and operational limitations of underwater robots and vehicles. Additionally, the metamaterial fabrication technique will benefit other underwater acoustic applications, such as underwater sensing, communication, biomedical diagnostics, therapy, and drug delivery.

Data availability statement

The data supporting the findings of this study are available within the article and its ESI. †

COMMUNICATION

Acoustic Metamaterials for Remote Manipulation of Large Objects in Water

Dajun Zhang[a] and Chu Ma [a] *

Received 00th January 20xx,
Accepted 00th January 20xx

DOI: 10.1039/x0xx00000x

Acoustic metamaterials have recently been applied to assist in the remote manipulation of objects in air, showing remarkable potential in alleviating the constraints of non-metamaterial-based acoustic manipulation methods regarding object size and the force's degree of freedom. To extend this approach to underwater manipulation, in this work, we develop a new type of underwater acoustic metamaterial based on a metal-resin composite, offering submillimeter scale feature resolution and high acoustic impedance contrast with water. By designing the surface patterns of the metamaterial, we demonstrate the remote acoustic manipulation of in-water large objects (>20 wavelengths) with 3D translational and rotational degrees of freedom. We then proposed two methods, surface pattern superimposition and frequency multiplexing, to integrate different manipulation forces within a single metamaterial patch. Additionally, we demonstrate more examples of complex object manipulation using multiple metamaterial patches and transducers, such as multi-object, multi-path, non-invasive, and 3D underwater manipulation. Our metamaterial-assisted remote underwater acoustic manipulation will have broad applications in underwater robot actuation, vehicle transportation, manufacturing, as well as in drug delivery and minimally invasive surgery.

1. Introduction

Acoustic metamaterials[1–4] are composite structures formed by unit cells with subwavelength sizes and exotic properties that do not exist in natural forms, e.g., negative mass density[5] and/or bulk modulus,[6–8] negative refractive index[9,10] and negative Poisson's ratio.[11,12] Acoustic metamaterials provide a variety of novel wave manipulation functionalities, e.g., phase/amplitude engineering,[13–15] super-resolution imaging,[9,16,17] impedance matching,[18,19] invisibility cloaking,[20,21] sound absorption,[22,23] unidirectional transparency, and nonreciprocal propagation.[24–26] These functions have offered powerful tools to solve the challenges in applications such as noise control, communications, medical diagnosis, and non-destructive testing.

Recently, acoustic metamaterials were applied to assist remote manipulation of large objects (i.e., objects greater than at least twice the wavelength) using acoustic waves.[27] When an acoustic wave is reflected by the object's surface, the exchange of momentum between the reflected and incident waves results in an acoustic radiation force on the object. By coating the object with a thin layer of acoustic metamaterial, the radiation force's spatial distribution can be controlled with subwavelength precision. Without the assistance of metamaterials, acoustic wave can only manipulate objects smaller or comparable to the wavelength. For example, particles can be tapped by acoustic standing waves at wave nodes and antinodes,[28–32] or at the potential wells generated by either a transducer array[33,34] or a hologram.[35,36] If the size of the object is large, the acoustic radiation force generated by the diffraction of a wave by the object has the magnitude and direction dependent on the object's surface shape and material properties, making it difficult to levitate and precisely manipulate the object. Only the levitation of large objects in particular symmetric shapes, such as spheres and flat plates, was previously demonstrated[37–41] without metamaterials. In contrast, acoustic metamaterials enable the manipulation of large objects with arbitrary sizes and shapes, by shaping the acoustic radiation force with subwavelength-sized surface patterns.

While metamaterial-assisted acoustic manipulation provides an intriguing prospect for large-object manipulation, it has only been demonstrated to manipulate an object in air.[27] To expand this approach to underwater manipulation, creating underwater acoustic metamaterials is a necessary but challenging step, mainly because of the small acoustic impedance contrast between water and most of the materials used in existing metamaterial construction, such as polymer-based resins[42] and soft materials.[43] Such small contrast cannot provide the required modulation to the acoustic radiation force for object manipulation. Metals or ceramics are viable material choices considering their relatively large acoustic impedance compared to water,[44,45] however, the fabrication capability of these two cannot provide sufficient resolution or shape complexity needed by metamaterials, not to mention the high cost.[46–49] The

[a] *Department of Electrical and Computer Engineering, University of Wisconsin–Madison, 1415 Engineering Drive, Madison, WI 53706, USA E-mail: chu.ma@wisc.edu*
† Electronic Supplementary Information (ESI) available. See
DOI: 10.1039/x0xx00000x

development of a low-cost, high-resolution solution to create underwater metamaterials will not only advance the remote acoustic manipulation, but also hold immense potential for applications of acoustic metamaterials in underwater sensing, communication, biomedical diagnosis, and therapy.[50,51]

In this work, we developed a new type of underwater acoustic metamaterial by fabricating subwavelength surface patterns using a metal-resin composite. Using the fabricated underwater metamaterial patches, we demonstrated remote acoustic manipulation of large objects in water with 3D translational and rotational degrees of freedom. We then developed two methods, surface pattern superimposition and frequency multiplexing, to achieve different manipulation functions within a single metamaterial patch. Additionally, we demonstrated more complex examples of multi-object, multi-path, non-invasive, and 3D underwater manipulation using multiple patches/transducers. Our metamaterial-assisted remote underwater acoustic manipulation has broad applications in underwater robot control and vehicle transportation, underwater assembly, as well as in drug delivery and minimally invasive surgery.

2. Results and discussion

2.1. Fabrication and characterization of underwater acoustic metamaterials

To achieve the required high acoustic impedance contrast with water, acoustic metamaterials are fabricated using a metal-resin composite created by mixing iron granules with Epoxy resin (see details in the Experimental Section). The iron granules have sizes in the range of 5-250 μm, which are smaller than the acoustic wavelength we are using (500-1500 μm for 1-3 MHz). Microscopic pictures of the metal-resin composite with different mass ratios of iron fillings are shown in Fig. 1(a). The measured density ρ and acoustic wave speed c of the composite are shown in Fig. 1(b). Because of the density difference between iron granules (~7800 kg·m^{-3}) and resin (~1500 kg·m^{-3}), the equivalent density of the composite increases as the mass ratio of the iron granules increases. The acoustic speed inside the composite remains roughly the same as the iron mass ratio increases. As a result, the acoustic impedance ($Z=\rho c$) increases from 2.89 MPa·S·m^{-3} to 13.8 MPa·S·m^{-3} as the iron mass ratio increases from 0% to 80%, leading to the increase of the acoustic reflection coefficient ($|R|=(Z_{mixture}-Z_{water})/(Z_{mixture}+Z_{water})$) from 0.3 to 0.8, as depicted in Fig. 1(c). More details regarding the acoustic property measurement are presented in Note S1 (ESI†).

Fig. 1(d) illustrates the steps to fabricate a metamaterial patch. Details of the fabrication process can be found in the Experimental Section. One fabricated sample with 80% iron granule mass ratio is pictured in Fig. 1(e). The 20 mm × 20 mm × 2 mm sample works for 1 MHz acoustic wave. It has surface patterns with the height ranging from 0 to 0.75 mm. This fabrication method can realize ~50 micrometre fabrication resolution. Our underwater metamaterials have the advantages of high spatial feature resolution, large acoustic impedance contrast with water, as well as low fabrication cost, promising for underwater and biomedical applications even beyond acoustic manipulation.

2.2. Design and demonstration of acoustic manipulation functions: pushing, rotating, following

As illustrated in Fig. 2(a), a metamaterial patch is attached to the bottom surface of the object that is floating on the water. The patch has a surface pattern with varying extrusion height. The

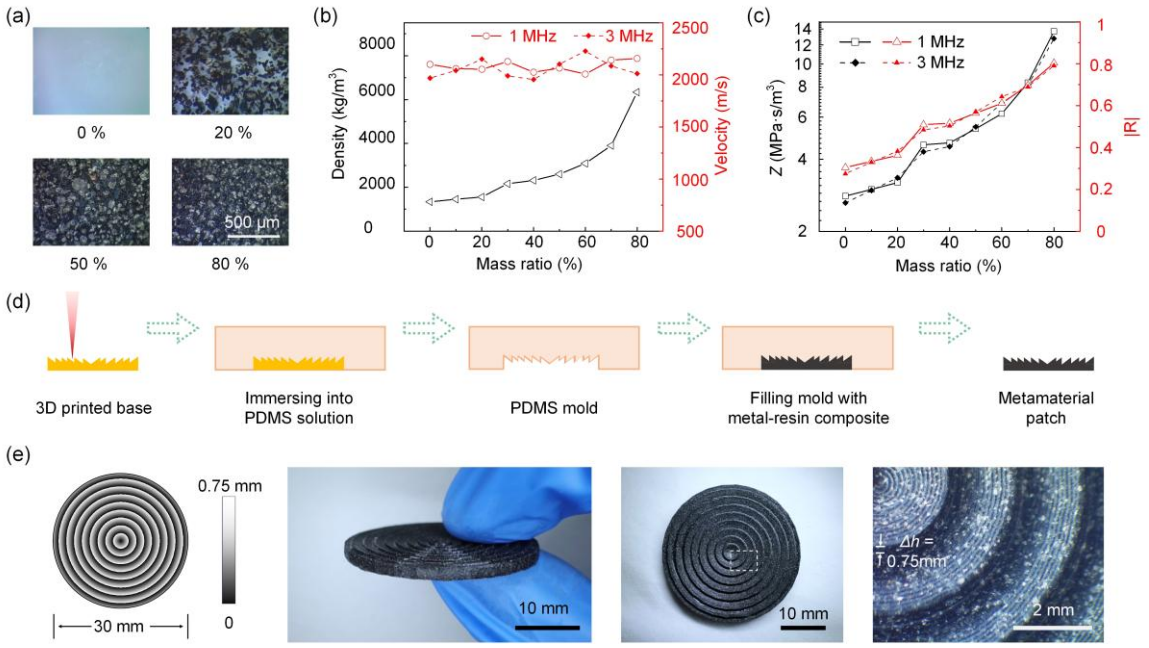

Fig. 1 Underwater acoustic metamaterial fabrication and characterization. (a) Microscopic photos of the metal-resin composite with different mass ratios of iron fillings. (b) The measured density and acoustic velocity for 1 MHz and 3 MHz acoustic wave of metal-resin composite samples with different iron filling ratios. (c) The calculated acoustic impedance and reflection coefficient of samples with different iron ratios. (d) Metamaterial patch fabrication process. (e) An example of the designed surface pattern, and the side-view, top-view, and microscopic top-view photos of a fabricated metamaterial patch.

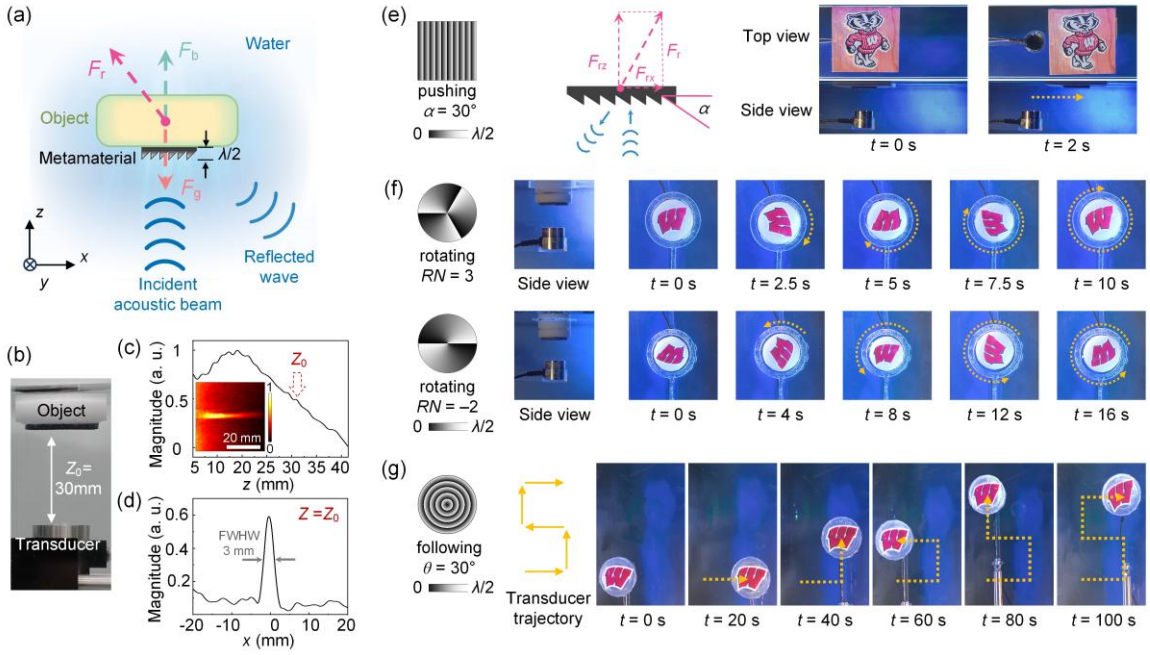

Fig. 2 Basic manipulation functions enabled by a metamaterial patch. (a) Illustration of the experimental setup and the forces involved. F_r: acoustic radiation force; F_b: buoyancy force; F_g: gravity force. (b) A side-view photo of the experiment setup. (c, d) Measured acoustic intensity of the incident beam along *z*- direction (c) and *x*- direction (d). The inset of (c) is the measured acoustic wave intensity in the *xz*-plane. (e-g) Designed surface patterns and snapshots of experimental movies for pushing (e), rotating (f), and following (g) functions enabled by metamaterial patches. The orange dash lines in the snapshots indicate the moving trajectories of the objects.

height gradient corresponds to the phase gradient of the reflected wave from the surface. The momentum exchange of the waves with the metamaterial surface generates an acoustic radiation force F_r on the object, whose direction and magnitude depend on the phase gradient. In an underwater environment, the other forces on the object are gravity F_g and buoyancy F_b, both in the *z* direction in the coordinate system shown in Fig. 2(a).

The incident acoustic beam is perpendicular to the metamaterial surface, emitted by an acoustic transducer with a center frequency of 1 MHz located 30 mm away from the metamaterial surface. We characterized the incident beam profile using a needle transducer and plotted the acoustic wave intensity along and perpendicular to the beam direction in Fig. 2(c) and 2(d). More details of acoustic beam characterization are in the Experimental Section. Fig. 2(d) shows that the incident acoustic beam has a width of around 3 mm at the Z_0 = 30 mm position.

The metamaterial surface patterns are designed to realize three basic manipulation functions: pushing, rotating, and following (Movie S1 (ESI†)). Combinations of these basic functions can realize more complex 3-D object manipulation.

2.2.1. Pushing

An *xy*-plane pushing force is generated by reflecting the *z*-direction incident acoustic beam to a direction that has a component in the *xy*-plane. The surface pattern height distribution in the *xy*-plane is designed as:

$$h_{\text{pushing}}=\text{mod}(\tan(\alpha)\cdot x, \lambda/2) \quad (1)$$

where α is the angle of the surface pattern with respect to the *x*-direction (and $-\alpha$ is the wave reflection angle), as shown in Fig. 2(e), and λ is the wavelength. Snapshots of the video showing the object moving in the *xy*-plane are also shown in Fig. 2(e).

To gain insight into the pushing mechanism, we experimentally measure the acoustic radiation force in the *z*-direction, F_{rz}, as a function of the reflection angle α. In underwater manipulation, the mass and volume of an object determine the magnitude of the buoyancy and gravity forces. At force equilibrium, the F_{rz} should equal the difference between the buoyancy and gravity. The experimental measurement of F_{rz} is performed in the following way: as the object is floated on the water surface, the immersion volume change of the object after the acoustic beam is turned on is proportional to F_{rz}. By constraining the object's *xy*-plane movement by a 3D printed ring-shape structure (left structure in Fig. S4 (ESI†)) and measuring its immersion volume change (ΔV), the F_{rz} can be calculated by $F_{rz} = \rho_{\text{water}} \cdot g \cdot \Delta V$, where g = 9.8 N·kg^{-1} and ρ_{water} = 10^3 kg·m^{-3} (Fig. S5(a) and Note S2 (ESI†)). In the F_{rz} measurements presented in Fig. 3(a), the same transducer input power of 3 W is applied and the acoustic wave reflection angle α varies from 0° to 60°. At each angle α, the measurement is repeated 20 times. The results indicate that the larger the reflection angle α, the smaller the F_{rz}. We also calculate the *xy*-direction and *z*-direction acoustic radiation forces, F_{rx} and F_{rz}, based on the theory of acoustic radiation force[52] and COMSOL modelling of the acoustic field distribution after the incident beam is reflected by the metamaterial patch (see more details in the Experimental Section and Note S3 (ESI†)). The normalized forces $F_{rx}/\max(F_{rz})$ and $F_{rz}/\max(F_{rz})$ from calculation are also plotted in Fig. 3(a). A similar decreasing trend as in experimental measurements is observed in the F_{rz} vs. α plot. At the same time, the calculated F_{rx} increases with α. The angle between the direction of the acoustic radiation force and the +*z* direction can be calculated by $\arctan(F_{rx}/F_{rz})$, which shows an increasing trend as the α become larger (shown in Fig. S7(e) (ESI†)). In Fig. S5(b)

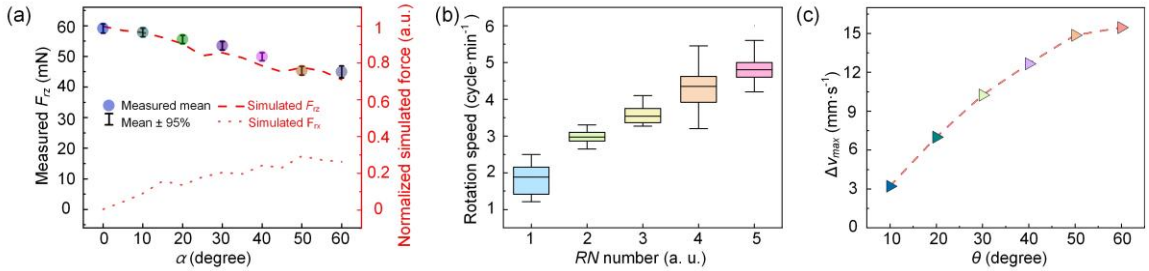

Fig. 3 Analysis of pushing, rotating and following functions. (a) In the "pushing" function, experimentally measured *z*-direction, and simulated *x*- and *z*-direction acoustic radiation forces as a function of reflection angle α. Error bars in the experimentally measured data represent 95% confidence interval. (b) In the "rotating" function, experimentally measured rotation speed as a function of *RN*, when keep incident beam power a constant (10 W). Box plots show the minimum, first quartile, median, third quartile, and maximum. (c) In the "following" function, experimentally measured largest speed change, Δv_{max}, of the object with "following" metamaterial (total weight 30 g) that the transducer (with 10 W input power) can induce as a function of ϑ.

(ESI†), we presented the measured F_{rz} as a function of the transducer input power, showing that magnitude of F_{rz} increases linearly with the transducer input power. We have also plotted the required F_{rz} as a function of the total mass and water-immersed volume of the object in Fig. S6(a) (ESI†). In addition to the mass and size of the object, the lateral size of the metamaterial patch also impacts the acoustic radiation force in both vertical and horizontal directions. On one hand, when using a focused ultrasound beam as in our experiments, the acoustic radiation force reaches its maximum at a specific transducer power as long as the lateral size of the metamaterial patch is slightly larger than the focal spot. On the other hand, a larger patch enables longer actuation time when the object moves, resulting in larger accumulative effect on the object's motion. A larger metamaterial patch is also heavier. In Fig. S6(b) (ESI†), we show the additional *z*-direction radiation forced needed because of the metamaterial patch as a function of the patch size.

2.2.2. Rotating

To generate a rotational force in the *xy*-plane by a *z*-direction acoustic beam, the height distribution of the surface pattern is designed as:

$$h_{\text{rotating}}=\text{mod}(RN\cdot\varphi\cdot\lambda/4\pi,\ \lambda/2), \quad (2)$$

where φ is the azimuth angle from 0 to 2π, and *RN* represents the number of periods along the azimuthal direction. In Fig. 2(f) and in Movie S1 (ESI†), two situations, $RN = 3$ and $RN = -2$ are shown. The metamaterial surface gives an angular momentum in the reflected wave, thus generating a rotational force to the object. The rotational motion is clockwise for positive *RN* and counterclockwise for negative *RN*. The rotating speed of the object is measured when metamaterial patches with different *RN* values are attached. During measurement, the object's translational movement is limited by a 3D printed ring-shaped structure (Fig. S4 (ESI†)). At each *RN* value, the measurement is repeated 20 times. As shown in Fig. 3(b), a larger *RN* magnitude produces a faster rotating speed (Movie S1 (ESI†))

2.2.3. Following

The "following" function, or object trapping, can be achieved by an axially symmetric surface pattern with a height distribution:

$$h_{\text{following}}=\text{mod}(\sin(\theta)\cdot\sqrt{\boldsymbol{x^2+y^2}},\ \lambda/2) \quad (3)$$

The acoustic radiation force at any point of the metamaterial surface has a *z*-component, F_{rz} that is perpendicular to the surface, and a transverse component, F_{rxy}, that is along the radial direction and points to the center of the surface. We name F_{rxy} the trapping force as it determines the capability of the metamaterial to trap and make the object following the transducer. The angle θ determines the ratio between F_{rxy} and F_{rz}. When the center of the acoustic beam and the center of the surface pattern overlap, the forces on the object are balanced because of the axial symmetry. As the acoustic beam center begins to move off the surface pattern center, for example to the left, the right-pointing force will become larger than the left-pointing one. The object will be forced to move left, following the movement of the acoustic beam center. In Fig. 2(b), we demonstrate that the object follows the transducer center and moves along an S-shape trajectory (also shown in Movie S1, ESI†).

To illustrate the relationship between the angle θ of the metamaterial surface pattern and the strength of the trapping force in the "following" function, we measured the largest speed change, Δv_{max}, of the object that the transducer can induce as a function of θ. An illustration of the measurement setup is in Fig. S5(c) (ESI†). The object is originally static while the transducer speed changes from 0 to Δv_{max} (acceleration). With the fixed transducer input power and object total weight, the increased angle θ in metamaterial design increases the Δv_{max}, which is due to the larger trapping force generated by the metamaterial (shown in Fig. 3(c)). We also show that with a fixed transducer input power, the Δv_{max} decreases with the object total weight (Fig. S5(d) (ESI†). This is because the acceleration decreases with the object mass.

2.3. Multifunctional design of a single metamaterial patch

In the above designs, a single metamaterial patch supports one manipulation function. Multifunctional design expands the manipulation capability provided by a single patch, thereby reducing the overall system complexity and manufacturing cost. Here we develop two mechanisms for multifunctional manipulation that are complementary to each other: surface pattern superimposition and frequency multiplexing.

2.3.1. Surface pattern superimposition

By superimposing two surface patterns, the metamaterial patch can provide two types of actuation forces to the object at the same time. As an example, in Fig. 4(a), the "pushing" and

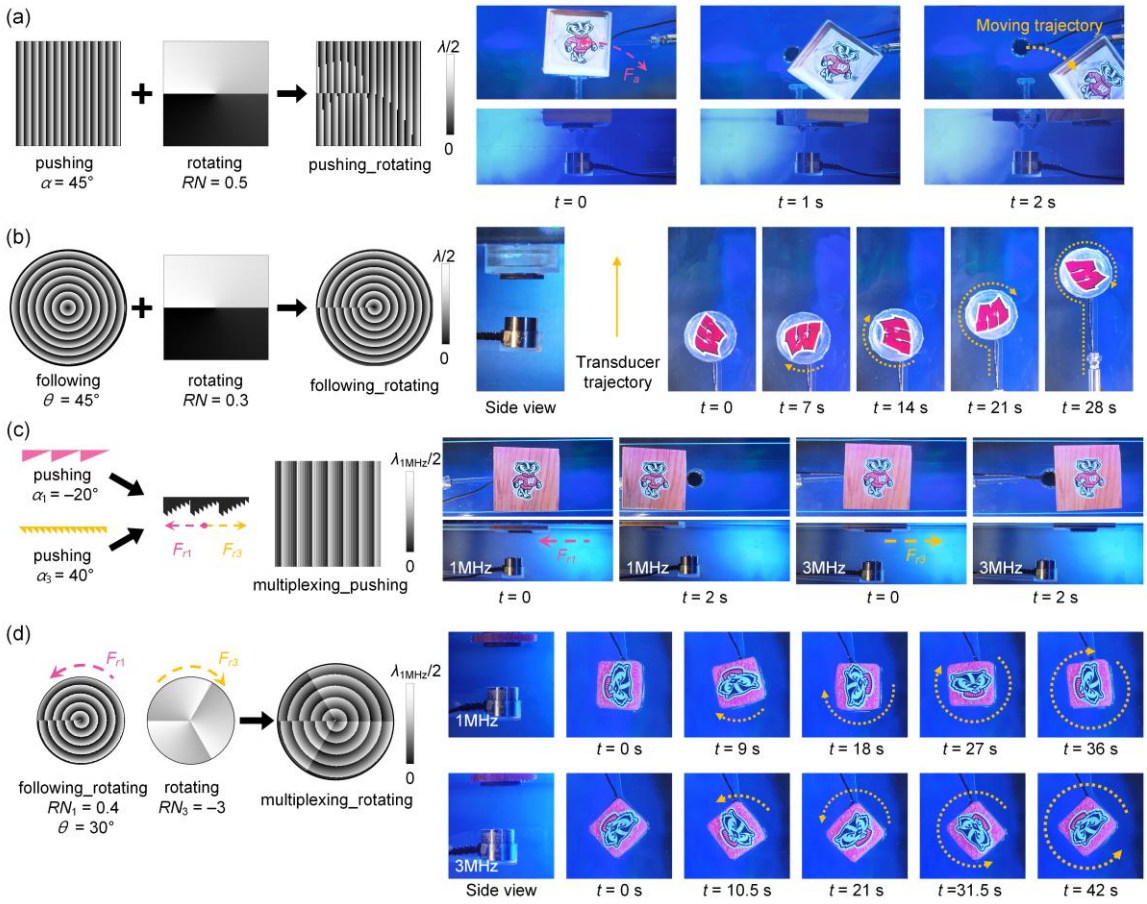

Fig. 4 Multifunctional pattern design and experiment verification. (a) Superimposition of pushing and rotating. (b) Superimposition of following and rotating. (c) Frequency multiplexing of right pushing at 1 MHz and left pushing at 3 MHz. (d) Frequency multiplexing of rotating following at 1 MHz and rotating at 3 MHz.

"rotating" patterns are superimposed, giving the pattern distribution as:

$$h_{\text{pushing\_rotating}}=\text{mod}(\tan(\alpha)\cdot x+RN\cdot\varphi\cdot\lambda/4\pi,\ \lambda/2) \quad (4)$$

The angle α is set as 45° and RN is set as 0.5. When an acoustic beam is incident onto the patch, the acoustic radiation force in the xy plane has two components: one along the x-direction and another rotating clockwise. Hence, the acoustic wave will push the object to move along a curved trajectory (Movie S2 (ESI†)).

In another example, we combine the "following" and "rotating" patterns (as shown in Fig. 4(b)) as:

$$h_{\text{following\_rotating}}=\text{mod}(\sin(\theta)\cdot\sqrt{x^2+y^2}+RN\cdot\varphi\cdot\lambda/4\pi,\ \lambda/2) \quad (5)$$

The angle θ is set to 45° and RN is set to 0.3. After turning on the acoustic incident beam, the object follows the movement of the beam and rotates clockwise at the same time (see Fig. 4(b) and Movie S2 (ESI†)).

2.3.2. Frequency multiplexing

Multifunctional manipulation can also be realized by frequency multiplexing. Acoustic reflection from a metamaterial patch is frequency dependent. The surface pattern designed for one frequency will generate a different radiation force distribution when interacts with acoustic beams in other frequencies. By superimposing multiple surface patterns that each only reacts to one single frequency among pre-selected frequency values, we can switch the acoustic radiation force among pre-designed distributions, leading to different object movements.

Our first example demonstrates the switching between two pushing directions using incident acoustic beams at 1 MHz and 3 MHz. We set the reflection angle as $\alpha_1 = -20°$ for 1 MHz, and $\alpha_3 = 40°$ for 3 MHz. The combined surface pattern distribution (Fig. 3(c)) is:

$$h_{\text{multiplexing\_pushing}} = \text{mod}(x\cdot\tan(\alpha_1), \lambda_1/2) + \text{mod}(x\cdot\tan(\alpha_3), \lambda_3/2) \quad (6)$$

where λ_1 and λ_3 are wavelengths at 1 MHz and 3 MHz, respectively. The surface pattern $h_{\text{multiplexing\_pushing}}$ reflects a 1 -MHz beam to the $+x$ half plane and a 3 -MHz beam to the $-x$ half plane, as shown in Fig. S8 (ESI†). Thus the 1 -MHz beam will push the object to the $-x$ direction with the generated radiation force F_{r1}, and the 3 -MHz beam will push the object to the $+x$ direction with F_{r3}, as shown by Movie S2 (ESI†), as well as the snapshots presented in Fig. 4(c).

In our second example, we demonstrate the switching between clockwise and counterclockwise rotation using 1-MHz and 3-MHz acoustic beams. The surface pattern is the combination of the following two designs: 1) the surface pattern superimposition of the "following" and "rotating" functions at 1 MHz, and 2) the "rotating" function at 3 MHz:

$$h_{\text{multiplexing\_rotating}} = \text{mod}(\sin(\theta)\sqrt{x^2+y^2}+RN_1\cdot\varphi\cdot\lambda_1/4\pi,\ \lambda_1/2) + \text{mod}(RN_3\cdot\varphi\cdot\lambda_3/4\pi,\lambda_3/2) \quad (7)$$

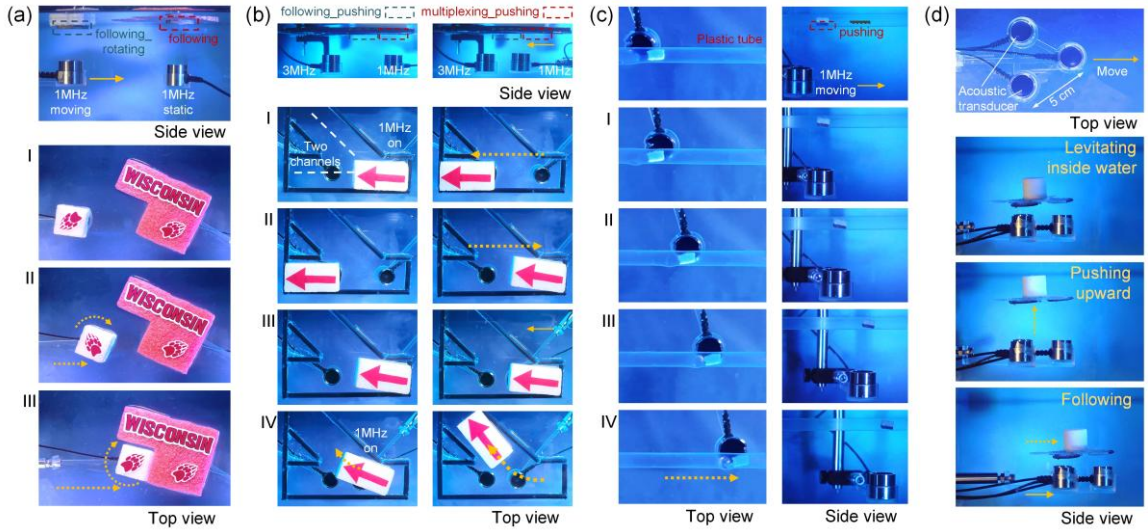

Fig. 5 Demonstration of complex object manipulation functions enabled by more than one metamaterial patches and transducers. (a) Multi-object manipulation. (b) Multi-path manipulation. (c) Non-invasive manipulation inside a tube. d) 3D manipulation in water. The experiment videos are shown in Movie S3.

where we set θ as 30°, RN_1 as 0.4 and RN_3 as –3. The 1-MHz and 3-MHz acoustic beams rotate the object clockwise and counterclockwise, respectively (Fig. 4(d) and Movie S2 (ESI†)). The surface pattern component $\sin(\theta)\sqrt{x^2+y^2}$ provides the trapping force to stabilize the object above the transducer.

2.4. Demonstration of complex underwater object manipulation

Our single- and multi-functional metamaterial patches enable many application scenarios for underwater acoustic object manipulation. We have already showed examples using a single patch, such as pushing, rotating, following, simultaneous following and rotating, simultaneous pushing and rotating, and frequency multiplexing of different functions. In this section we demonstrate several more complex scenarios that require the cooperation of more than one patch and transducer pair. The results are presented in Fig. 5 and Movie S3 (ESI†).

2.4.1. Multi-object manipulation

In the first example, we demonstrate multi-object manipulation for underwater assembly of parts, as shown in Fig. 5(a). A "following_rotating" patch is attached to the left object and a "following" patch is attached to the right object (shown in Fig. S9(a) (ESI†)). A transducer moves and rotates the left object towards the right one, which is trapped to its original location by a second transducer. The two objects get assembled as they get close (stages I to III in Fig. 5(b)).

2.4.2. Multi-path manipulation

In the second example, one metamaterial patch with the "pushing_rotating" function and another with "multiplexing_pushing" function are attached to an object (shown in Fig. S9(b) (ESI†)). Two acoustic transducers providing 1 -MHz and 3 -MHz beams are placed at two separate locations. At the stage I in Fig. 5(b), the 1-MHz transducer at the location of the "multiplexing_pushing" patch is turned on, pushing the object to the left along the horizontal channel. At stage II, the 3-MHz transducer is turned on, now facing the "multiplexing_pushing" patch and providing a right-direction force to the object. At stage III, the 1-MHz transducer is moved to the position of the "pushing_rotating" patch working at 1 MHz. When the 1-MHz transducer is turned on at stage IV, the object is pushed along a curved trajectory into another channel branch.

2.4.3. Non-invasive manipulation inside a tube

Acoustic waves can penetrate through walls/obstacles non-invasively. In the second example, we demonstrate the remote manipulation of an object inside a tube merged in water (Fig. S9(c) (ESI†)). As shown in Fig 5(c), the object with a metamaterial patch that supports the pushing function can be moved along a tube by a transducer pointing to the patch (stages I to IV in Fig. 5(c)).

2.4.4. 3D manipulation in water

In the last example, we show 3D manipulation of an object fully submerged in water. Three "following" patches are attached at the bottom of the object (Fig. S9(d) (ESI†)), each has a transducer facing it (shown in the top row of Fig. 5(d)). The total volume of the metamaterial patch and the object is estimated as ~15cm^3, giving the buoyancy of ~150 mN. And the total weight is 20.37g, corresponding to the gravity of ~200 mN. In our setup, when the input power of the transducers is 3 W, the buoyancy, gravity, and the acoustic radiation forces reach a balance state. As shown in Movie S3 (ESI†), the object is levitated 30 mm away from the transducers and follows the movement of the transducers. When the input power is larger than 3 W, the object moves towards the positive *z* direction. When the input power is smaller than 3 W, the object moves towards the negative z-direction. Three patch-transducer pairs are needed to stabilize the object at its levitated position and during motion.

3. Conclusions

In this study, we developed acoustic metamaterial to tailor the acoustic radiation force for multi-degree-of-freedom

manipulation of large objects (>20 wavelengths) in water. The metamaterial fabricated through soft lithography of iron-resin mixtures have the advantages of large acoustic impedance contrast with water, sub-millimeter spatial feature resolution, and low fabrication cost, which are highly demanded in underwater applications of metamaterials, including sensing, communication, and actuation. In our work, we explored its application in enabling underwater acoustic remote manipulation of large objects. We developed basic manipulation functions including pushing, rotating, and following. We also developed two methods, surface pattern superimposition and frequency multiplexing, to combine different basic manipulation functions onto a single metamaterial patch, such as pushing and rotating, rotating and following, left and right pushing, and clockwise and counterclockwise rotating. Furthermore, we demonstrated application-driven examples of complex underwater object manipulation by the collaboration of more than one metamaterial patches and transducers.

In our metamaterial-assisted remote acoustic manipulation, the size of the object is no longer limited by the acoustic wavelength. We can exert controllable forces on underwater objects with sizes much larger than the used acoustic wavelength, which was difficult in previously established acoustic manipulation approaches based on standing wave or acoustic pressure gradient. As acoustic wave can penetrate through materials non-invasively, our system can also be used to manipulate objects inside containers and behind obstacles. In future works, the metamaterial patches can be made soft and conformable to different object surface shapes. The metamaterial structure can be designed so that the manipulation function is switchable with different incident wave angles or wavefront shapes. The metamaterial can also be made of reconfigurable materials, so that the manipulation function can be changed with environmental stimuli. Moreover, we can attach multiple patches at different locations of the object, each implementing a different movement. Feedback control through imaging of the object position and trajectory can be added to the system to generate more stable object motion, and also enable real-time motion planning. Our work will have broad applications in the control of underwater robots and unmanned vehicles, underwater assembly, minimally invasive surgery, and drug delivery.

4. Experimental section

4.1. Metamaterial fabrication and characterization

The metamaterial patches were fabricated through a soft lithography process. First, a resin base (Formlabs Clear Resin) was fabricated by a 3D printer (Form 3, Formlabs Inc.). Then the resin base was immersed into PDMS liquid (10:1 volume ratio, Sylgard 186 Silicone Elastomer Kit). After heating at 80 degrees for 60 minutes, the PDMS mold with inversed patterns was separated from the resin base. The metal-resin mixture, prepared by mixing iron granules (Bulk Iron Filings, by American Heritage Industries) with resin gel (Epoxy crystal clear Resin Kit, PIXISS) at pre-designed weight ratios, was then filled into the PDMS mold. After 12 hours of curing in room temperature, the ready-to-use metamaterial patch was separated from the PDMS mold. The metamaterial patches used in experiments are shown in Fig. S1 (ESI†).

We also fabricated 4 cm × 4 cm × 1 cm samples with different iron filling weight ratios to measure the acoustic properties. The density of these samples was calculated using the mass and volume, and acoustic velocities of the used 1 MHz and 3 MHz acoustic waves were measured through the wave transmission experiment (more in the Note S1 (ESI†)).

4.2. Acoustic field simulation and acoustic radiation force calculation

The spatial distribution of acoustic field generated by the reflection of an acoustic beam by a metamaterial patch is simulated using the Pressure Acoustics module in COMSOL Multiphysics 6.0. The acoustic radiation force exerted on the object was calculated by the equation[52,53]

$$\overrightarrow{F_r} = -\oint \left\{ \left[\frac{1}{2}\kappa_0 \langle p^2 \rangle - \frac{1}{2}\rho \langle \vec{u}^2 \rangle \right] \vec{n} + \rho \langle (\vec{n}\cdot\vec{u})\vec{u} \rangle \right\} da \qquad (8)$$

where κ0 is the compressibility $\kappa_0=1/(\rho c_2)$, ρ is the density of water and c is the acoustic wave speed in water. The p and $\vec{u}$ are the acoustic pressure and acoustic velocity of the wave. The integration is performed along a boundary enclosing the object. More details of the simulation and acoustic radiation force calculation are in Note S3 and Fig. S7 (ESI†).

4.3. Acoustic manipulation experiments

The materials of the objects used in the experiments include wood, wax, 3D-printed resin, plastic foam, and PDMS. The metamaterial patch was fixed on an object and was placed at the focal spot of a high-intensity focused ultrasound (HIFU) transducer (focal length: 30 mm). Two HIFU transducers, TQ20-1030 and TQ20-3030 from Siansonic Inc., are used to generate 1 -MHz and 3 -MHz beams, respectively. The HIFU transducers are controlled by a function generator (AFG3022C, Tektronix Inc.) and a power amplifier (AD1006, T&C Power Conversion) to specify the frequency and power of the incident beam. A needle hydrophone (Precision Acoustics NH0075) mounted on a 3D translation stage was used to characterize the field distribution of the beam (Fig. S3 (ESI†)). More details of the metamaterial patches, objects, and input power of the transducer are listed in Table S1 (ESI†).

Author contributions

D. Z. and C. M. proposed the project and conceived the idea. D. Z. designed and carried out the experiments. D. Z. and C. M. analyzed the data and wrote the manuscript. C. M. supervised the project.

Data availability

The data supporting the findings of this study are available within the article and its ESI. †

Conflicts of interest

There are no conflicts to declare.

Acknowledgements

This work was supported by National Science Foundation under Grant No. 2328096.

Notes and references

1 S. A. Cummer, J. Christensen and A. Alù, *Nat Rev Mater*, 2016, **1**, 16001.
2 H. Ge, M. Yang, C. Ma, M.-H. Lu, Y.-F. Chen, N. Fang and P. Sheng, *National Science Review*, 2018, **5**, 159–182.
3 J. Liu, H. Guo and T. Wang, *Crystals*, 2020, **10**, 305.
4 G. Ma and P. Sheng, *Sci. Adv.*, 2016, **2**, e1501595.
5 S. H. Lee, C. M. Park, Y. M. Seo, Z. G. Wang and C. K. Kim, *Physics Letters A*, 2009, **373**, 4464–4469.
6 N. Fang, D. Xi, J. Xu, M. Ambati, W. Srituravanich, C. Sun and X. Zhang, *Nature Mater*, 2006, **5**, 452–456.
7 S. H. Lee, C. M. Park, Y. M. Seo, Z. G. Wang and C. K. Kim, *Phys. Rev. Lett.*, 2010, **104**, 054301.
8 M. Yang, G. Ma, Z. Yang and P. Sheng, *Phys. Rev. Lett.*, 2013, **110**, 134301.
9 N. Kaina, F. Lemoult, M. Fink and G. Lerosey, *Nature*, 2015, **525**, 77–81.
10 Z. J. Wong, Y. Wang, K. O'Brien, J. Rho, X. Yin, S. Zhang, N. Fang, T.-J. Yen and X. Zhang, *J. Opt.*, 2017, **19**, 084007.
11 S. Babaee, J. Shim, J. C. Weaver, E. R. Chen, N. Patel and K. Bertoldi, *Advanced Materials*, 2013, **25**, 5044–5049.
12 X. Hou and V. V. Silberschmidt, in *Mechanics of Advanced Materials: Analysis of Properties and Performance*, eds. V. V. Silberschmidt and V. P. Matveenko, Springer International Publishing, Cham, 2015, pp. 155–179.
13 Y. Li, C. Shen, Y. Xie, J. Li, W. Wang, S. A. Cummer and Y. Jing, *Phys. Rev. Lett.*, 2017, **119**, 035501.
14 B. Xie, K. Tang, H. Cheng, Z. Liu, S. Chen and J. Tian, *Advanced Materials*, 2017, **29**, 1603507.
15 Y. Xie, W. Wang, H. Chen, A. Konneker, B.-I. Popa and S. A. Cummer, *Nat Commun*, 2014, **5**, 5553.
16 J. Zhu, J. Christensen, J. Jung, L. Martin-Moreno, X. Yin, L. Fok, X. Zhang and F. J. Garcia-Vidal, *Nature Phys*, 2011, **7**, 52–55.
17 M. Molerón and C. Daraio, *Nat Commun*, 2015, **6**, 8037.
18 G. D'Aguanno, K. Q. Le, R. Trimm, A. Alù, N. Mattiucci, A. D. Mathias, N. Aközbek and M. J. Bloemer, *Sci Rep*, 2012, **2**, 340.
19 Y. Xie, A. Konneker, B.-I. Popa and S. A. Cummer, *Appl. Phys. Lett.*, 2013, **103**, 201906.
20 H. Chen and C. T. Chan, *J. Phys. D: Appl. Phys.*, 2010, **43**, 113001.
21 S. Zhang, C. Xia and N. Fang, *Phys. Rev. Lett.*, 2011, **106**, 024301.
22 J. Mei, G. Ma, M. Yang, Z. Yang, W. Wen and P. Sheng, *Nat Commun*, 2012, **3**, 756.
23 M. Yang, C. Meng, C. Fu, Y. Li, Z. Yang and P. Sheng, *Applied Physics Letters*, 2015, **107**, 104104.
24 C. Shi, M. Dubois, Y. Chen, L. Cheng, H. Ramezani, Y. Wang and X. Zhang, *Nat Commun*, 2016, **7**, 11110.
25 X. Zhu, H. Ramezani, C. Shi, J. Zhu and X. Zhang, *Phys. Rev. X*, 2014, **4**, 031042.
26 R. Fleury, D. Sounas and A. Alù, *Nat Commun*, 2015, **6**, 5905.
27 M. Stein, S. Keller, Y. Luo and O. Ilic, *Nat Commun*, 2022, **13**, 6533.
28 H. M. Hertz, *Journal of Applied Physics*, 1995, **78**, 4845–4849.
29 X. Ding, S.-C. S. Lin, B. Kiraly, H. Yue, S. Li, I.-K. Chiang, J. Shi, S. J. Benkovic and T. J. Huang, *Proc. Natl. Acad. Sci. U.S.A.*, 2012, **109**, 11105–11109.
30 D. J. Collins, B. Morahan, J. Garcia-Bustos, C. Doerig, M. Plebanski and A. Neild, *Nat Commun*, 2015, **6**, 8686.
31 J. Li, C. Shen, T. J. Huang and S. A. Cummer, *Sci. Adv.*, 2021, **7**, eabi5502.
32 V. M. Jooss, J. S. Bolten, J. Huwyler and D. Ahmed, *Sci. Adv.*, 2022, **8**, eabm2785.
33 A. Marzo and B. W. Drinkwater, *Proc. Natl. Acad. Sci. U.S.A.*, 2019, **116**, 84–89.
34 A. Marzo, S. A. Seah, B. W. Drinkwater, D. R. Sahoo, B. Long and S. Subramanian, *Nat Commun*, 2015, **6**, 8661.
35 K. Melde, A. G. Mark, T. Qiu and P. Fischer, *Nature*, 2016, **537**, 518–522.
36 Z. Ma, A. W. Holle, K. Melde, T. Qiu, K. Poeppel, V. M. Kadiri and P. Fischer, *Adv. Mater.*, 2020, **32**, 1904181.
37 M. A. B. Andrade, A. L. Bernassau and J. C. Adamowski, *Applied Physics Letters*, 2016, **109**, 044101.
38 M. A. B. Andrade, F. T. A. Okina, A. L. Bernassau and J. C. Adamowski, *The Journal of the Acoustical Society of America*, 2017, **141**, 4148–4154.
39 S. Zhao and J. Wallaschek, *Arch Appl Mech*, 2011, **81**, 123–139.
40 D. Foresti, M. Nabavi, M. Klingauf, A. Ferrari and D. Poulikakos, *Proc. Natl. Acad. Sci. U.S.A.*, 2013, **110**, 12549–12554.
41 C. E. M. Démoré, P. M. Dahl, Z. Yang, P. Glynne-Jones, A. Melzer, S. Cochran, M. P. MacDonald and G. C. Spalding, *Phys. Rev. Lett.*, 2014, **112**, 174302.
42 L. J. Tan, W. Zhu and K. Zhou, *Adv Funct Materials*, 2020, **30**, 2003062.
43 H. Lim, H. S. Kim, R. Qazi, Y. Kwon, J. Jeong and W. Yeo, *Advanced Materials*, 2020, **32**, 1901924.

44 C. W. Cushing, P. S. Wilson, M. R. Haberman, C. Shen, J. Li, S. A. Cummer, Z. J. Tan, C. Ma, H. Du and N. X. Fang, *The Journal of the Acoustical Society of America*, 2021, **149**, 1829–1837.
45 H. Li, Z. D. Deng and T. J. Carlson, *sens lett*, 2012, **10**, 679–697.
46 Y. Bi, H. Jia, Z. Sun, Y. Yang, H. Zhao and J. Yang, *Applied Physics Letters*, 2018, **112**, 223502.
47 M. Y. Wang, M. Thevamaran, M. S. Mattei, B. G. Hacha, G. A. Mazzei Capote, Z. Yu, T. Osswald, R. H. Goldsmith, D. J. Thoma and C. Ma, *Appl. Phys. Lett.*, 2022, **120**, 141702.
48 Y.-X. Shen, Y.-G. Peng, F. Cai, K. Huang, D.-G. Zhao, C.-W. Qiu, H. Zheng and X.-F. Zhu, *Nat Commun*, 2019, **10**, 3411.
49 C. Shen, C. Rohde, C. W. Cushing, J. Li, Z. J. Tan, H. Du, X. Peng, P. S. Wilson, M. R. Haberman, N. X. Fang and S. A. Cummer, *Adv Eng Mater*, 2023, **25**, 2201294.
50 E. Dong, P. Cao, J. Zhang, S. Zhang, N. X. Fang and Y. Zhang, *National Science Review*, 2023, **10**, nwac246.
51 J. Zhang, B. Hu and S. Wang, *Applied Physics Letters*, 2023, **123**, 010502.
52 H. Bruus, *Lab Chip*, 2012, **12**, 1014.
53 M. Settnes and H. Bruus, *Phys. Rev. E*, 2012, **85**, 016327.